



Pd single-atom decorated CdS nanocatalyst for highly efficient overall water splitting under simulated solar light

Wei Li^{a,*}, Xiao-shan Chu^a, Fei Wang^a, Yan-yan Dang^a, Xiao-yun Liu^a, Teng-hao Ma^a, Jia-yuan Li^a, Chuan-yi Wang^{b,**}

^a College of Chemistry and Chemical Engineering, Shaanxi Key Laboratory of Chemical Additives for Industry, Shaanxi University of Science & Technology, Xi'an, Shaanxi 710021, China

^b School of Environmental Sciences and Engineering, Shaanxi University of Science & Technology, Xi'an, Shaanxi 710021, China

ARTICLE INFO

Keywords:

Palladium single-atom
Hexagonal CdS
Overall water splitting
Hydrogen production
Simulated-solar-light

ABSTRACT

Solar-induced overall water splitting to produce hydrogen is inspiring towards energy sustainability, but it is also formidable due to its limited efficiency seriously hindering its scale up for practical application. CdS is an important transition metal sulfide with low-work-function. However, its photostability is often deteriorated due to photocorrosion influence. To overcome this issue, single-atom Pd was employed here to decorate CdS to form a CdS-Pd nanocatalyst through a simple and controllable photoinduced reduction strategy. The synergetic semiconductor (CdS)-metal (Pd) interaction promotes the fast bulk-to-surface electron migration, thereby the resultant CdS-Pd (3.83%) nanocatalyst shows considerable structural stability and dramatically improved solar-induced HER activity in overall water splitting, about 110-fold higher than that of pristine CdS. Meanwhile, high apparent quantum yields (AQYs) of 4.47%/1.81% and 33.92%/27.49% were respectively achieved with this decorated nanocatalyst under the light of 420 nm/500 nm in absence and presence of scavenger, demonstrating the high-efficiency under broadband light illumination. Density functional theory (DFT) calculation supports that the easy formation of H^{*} intermediates on the decorated nanocatalyst due to low energy barriers accounts for the internal promoted mechanism for hydrogen production. This study provides important insight to gain stable CdS-based photocatalysts for high-efficient hydrogen production by overall water splitting.

1. Introduction

Hydrogen evolution reaction (HER) is a typical half-reaction for producing hydrogen energy. However, conventional hydrogen production generally results in massive emission of greenhouse gas or high energy consumption, making it extremely urgent to develop cleaner production approaches [1]. Photoinduced water splitting to produce hydrogen is a promising strategy for solving urgent energy problem, but the poor photoresponse and weak interfacial electronic transportation hinder the application of numerous semiconductor photocatalysts in large-scale hydrogen production [2].

Cadmium sulfide (CdS), a typical transition metal sulfide (TMS) with low-work-function and prominent solar-response, is a promising candidate to acquire high-efficient HER activity under simulated-solar-light (SSL) [3]. However, pure CdS semiconductor generally presents

weak structural stability for serious photocorrosion under long-term illumination, seriously influencing its photocatalytic performance. Meanwhile, nanomaterial toxicity due to heavy metal ions releasing in application also requires special attention [4]. Notably, some high-efficient CdS-based photocatalysts have been exploited successively, but their synthetic methods are generally very complicated and hard to operate.

In view of the unique electronic structure and unsaturated coordination environment of metallic single-atom sites (SASs), they are widely used to improve the catalytic performance of semiconductor catalysts for exposing of abundant active sites and higher atomic availability [5]. For instance, Tiwari et al. [6] decorated Pd SASs on Co₂P NPs, and Wang et al. [7] loaded Ir SASs on NiO matrix. Moreover, TiO₂-based catalysts were successively decorated by single-atomic Cu [8], Pt [9], and Pd [10] etc. CdS-based catalysts were successively decorated by single-atomic Pt

* Correspondence to: College of Chemistry and Chemical Engineering, Key Laboratory of Auxiliary Chemistry and Technology for Chemical Industry, Ministry of Education, Shaanxi Key Laboratory of Chemical Additives for Industry, Shaanxi University of Science & Technology, Xi'an, Shaanxi 710021, China.

** Corresponding author.

E-mail addresses: liweihg@sust.edu.cn (W. Li), wangchuan-yi@sust.edu.cn (C.-y. Wang).

<https://doi.org/10.1016/j.apcatb.2021.121000>

Received 18 November 2021; Received in revised form 30 November 2021; Accepted 5 December 2021

Available online 8 December 2021

0926-3373/© 2021 Elsevier B.V. All rights reserved.

[11], Ru [12], Pd [13], Au [14] etc. Also, C_3N_4 -based catalysts were successively decorated by single-atomic Fe [15], Ni [16], Cu [17], Ag [18], Au [19], Pt [20], Pd [21], Co [22] etc. Additionally, Shi et al. [23] decorated Co SASs on a porous carbon matrix, and Zuo [24] and Wang et al. [25] loaded Pt and Cu SASs on metal-organic frameworks (MOFs), and Huang [26] and Sun et al. [27] respectively anchored molybdenum and Pt SASs on N-doped graphene. Notably, SASs decoration can effectively improve the catalytic performance and enhance structural stability of conventional catalysts [28], even realizing hydrogen production through overall water splitting under photoirradiation due to synergetic host-guest interaction [29].

However, a great challenge remaining in metallic single atom catalysts is stability, which is because single atom tends to aggregate due to its high surface energy. In view of this character, a strategy based on metal-semiconductor interaction was developed to obtain stable single atomic Pd decorated CdS nanocatalyst. Due to the synergetic semiconductor (CdS)-metal (Pd) interaction, the fast bulk-to-surface electron migration is achieved, thus the resultant CdS-Pd (3.83%) nanocatalyst shows considerable structural stability and about 110-fold higher SSL-induced HER activity of pristine CdS in overall water splitting, and achieves high AQYs of 4.47%/1.81% and 33.92%/27.49% under the light of 420 nm/500 nm in absence and presence of scavenger, respectively, demonstrating the high-efficiency of CdS-Pd (3.83%) nanocatalyst under broadband light illumination. Density functional theory (DFT) calculations demonstrates the easy formation of H^+ intermediates on the decorated nanocatalyst due to low energy barriers, which further explains the internal promoted mechanism for hydrogen production. This study provides an important insight to gain stable CdS-based photocatalyst for high-efficient hydrogen production by overall water splitting.

2. Methods

2.1. Catalyst preparation

The CdS NPs were synthesized according to the method in [Supplementary Material](#). The CdS-Pd nanocatalyst was synthesized via a simple photoinduced reduction strategy. In detail, a moderate proportion of CdS NPs and $PdCl_2$ (AR) were dispersed and dissolved in 50 mL deionized water. After degassing treatment, the mixture was illuminated (300 W xenon lamp) for 1 h under constantly stirring. Then, the product was centrifuged and dried at 70 °C, and the resultant brown powder was the CdS-Pd nanocatalyst. The amount of palladium species was confirmed by ICP-MS (ICPA 6000 SERIES, US) analysis.

2.2. Characterization

The crystal phases and structures of the catalysts were analyzed on X-ray diffractometer (XRD, Bruker D8 Advance, UK), Raman imaging spectrometer (THEM, DXRxi, US), and spherical aberration correction transmission electron microscope (ac-TEM, Hitachi, JEM-ARM300F, JPN). The compositions and surface chemical states of the catalysts were analyzed on X-ray photoelectron spectroscopy (XPS, Axis Supra, UK). The photochemical properties of the catalysts were analyzed on UV-vis-NIR spectrometer (Agilent, Cary 5000, US) and fluorescence spectrometer (Edinburgh FS5, UK). The electrochemical measurements were performed on a electrochemical analyzer (CHI660E, CN). The radicals were analyzed on an electron paramagnetic resonance (EPR) spectrometer (Bruker A300, GER).

2.3. Overall water splitting for HER

The HER activity in overall water splitting was evaluated on a Labsolar-III AG system (Beijing Perfect Light Technology Co., CN). Briefly, 10 mg catalyst was dispersed in 50 mL deionized water, then it was situated at 5 °C and illuminated by a 300 W xenon lamp (PLS-SXE

300) after degassing for 10 min. The amount of hydrogen was measured per hour on a gas chromatograph (GC7900, TianM, CN). Also, the HER activity was also evaluated at the presence of triethanolamine (TEOA, 15 vol%).

2.4. Photo-electrochemical property tests

All photo-electrochemical properties were tested on a CHI660 electrochemical analyzer through a three-electrode system [30]. The detailed parameters are given in [Supplementary Material](#).

2.5. Computational details

All density functional theory (DFT) calculations were performed within the generalized gradient approximation (GGA) based on the Vienna Ab Initio Package (VASP) [31]. We have employed the Vienna Ab Initio Package (VASP) to perform all the density functional theory (DFT) calculations within the generalized gradient approximation (GGA) using the PBE formulation [32]. The detailed calculation method is given in [Supplementary Material](#).

3. Results and discussion

3.1. Microstructure and composition

Fig. 1a illustrates the preparation of CdS-Pd nanocatalyst. Briefly, a specific amount of $PdCl_2$ was dissolved in uniform aqueous CdS NPs dispersion to synthesize CdS-Pd nanocatalyst via a surface photoinduced reduction strategy, and the dosage of Pd species was determined by inductively coupled plasma mass spectrometry (ICP-MS, ICPA 6000 SERIES, US) analysis. As formed CdS-Pd (3.83%) nanocatalyst was optimized according to its HER activity in overall water splitting (**Fig. S1**) X-ray photoelectron spectroscopy (XPS) was performed to determine the elemental composition of the CdS-Pd (3.83%) nanocatalyst and its chemical states. The survey spectra in **Fig. S2** indicates the CdS-Pd (3.83%) nanocatalyst is composed of Cd, S and Pd elements, revealing the successful decoration of Pd species on the surface of CdS NPs. Compared with pure CdS NPs, two characteristic peaks assigned to Cd $3d_{3/2}$ (411.95 eV) and Cd $3d_{5/2}$ (405.25 eV) orbitals of Cd^{2+} state do not appear obvious shifts (**Fig. 1b**), but the slight peak shifts of S $2p_{3/2}$ (+0.06 eV) and S $2p_{1/2}$ (+0.05 eV) orbitals to higher binding energy are presented in **Fig. 1c** after Pd decoration, implying the formation of strong S-Pd bonding interaction on the surface of CdS-Pd (3.83%) nanocatalyst [33]. Furthermore, two characteristic peaks assigned to the Pd $3d_{3/2}$ (343.24 eV) and Pd $3d_{5/2}$ (337.32 eV) orbitals of Pd(0) state and two characteristic peaks assigned to Pd $3d_{3/2}$ (340.85 eV) and Pd $3d_{5/2}$ (335.54 eV) orbitals of Pd(II) state simultaneously appear in Pd 3d high-resolution spectrum (**Fig. 1d**), suggesting the coexistence of Pd species on the surface of CdS NPs in two valent states. **Fig. S3** shows the corresponding X-ray diffraction (XRD) patterns. The similar hexagonal crystallization of CdS (PDF#41-1049) [34] is presented in the XRD pattern of CdS-Pd (3.83%) nanocatalyst, and the diffraction peaks assigned to Pd species are absent in its XRD pattern, suggesting the ultrafine dispersion of Pd species on the surface of CdS NPs in ultra-low content (3.83%). Then, Raman analysis was performed to further demonstrate the interaction between CdS NPs and Pd species. **Fig. 1e** shows that the intensity ratio of the first-order longitudinal optical (1-LO) mode (294 cm^{-1}) and second-order (2-LO) mode (593 cm^{-1}) of CdS-Pd (3.83%) nanocatalyst ($I_1/I_2 = 2.75$) is very different from that of pure CdS NPs ($I_1/I_2 = 2.80$), [35], implying the formation of strong CdS-Pd interaction, and this conclusion is consistent with XPS analysis.

The microstructures of pure CdS NPs and CdS-Pd (3.83%) nanocatalyst were characterized by aberration-corrected high-annular dark-field scanning TEM (AC HAADF-STEM) as displayed in **Fig. 2a** and **c**, and the lattice fringes of $d = 0.36\text{ nm}$ in **Fig. 2a** are assigned to the (100) crystal plane of hexagonal CdS [36]. Notably, Pd SASs uniformly

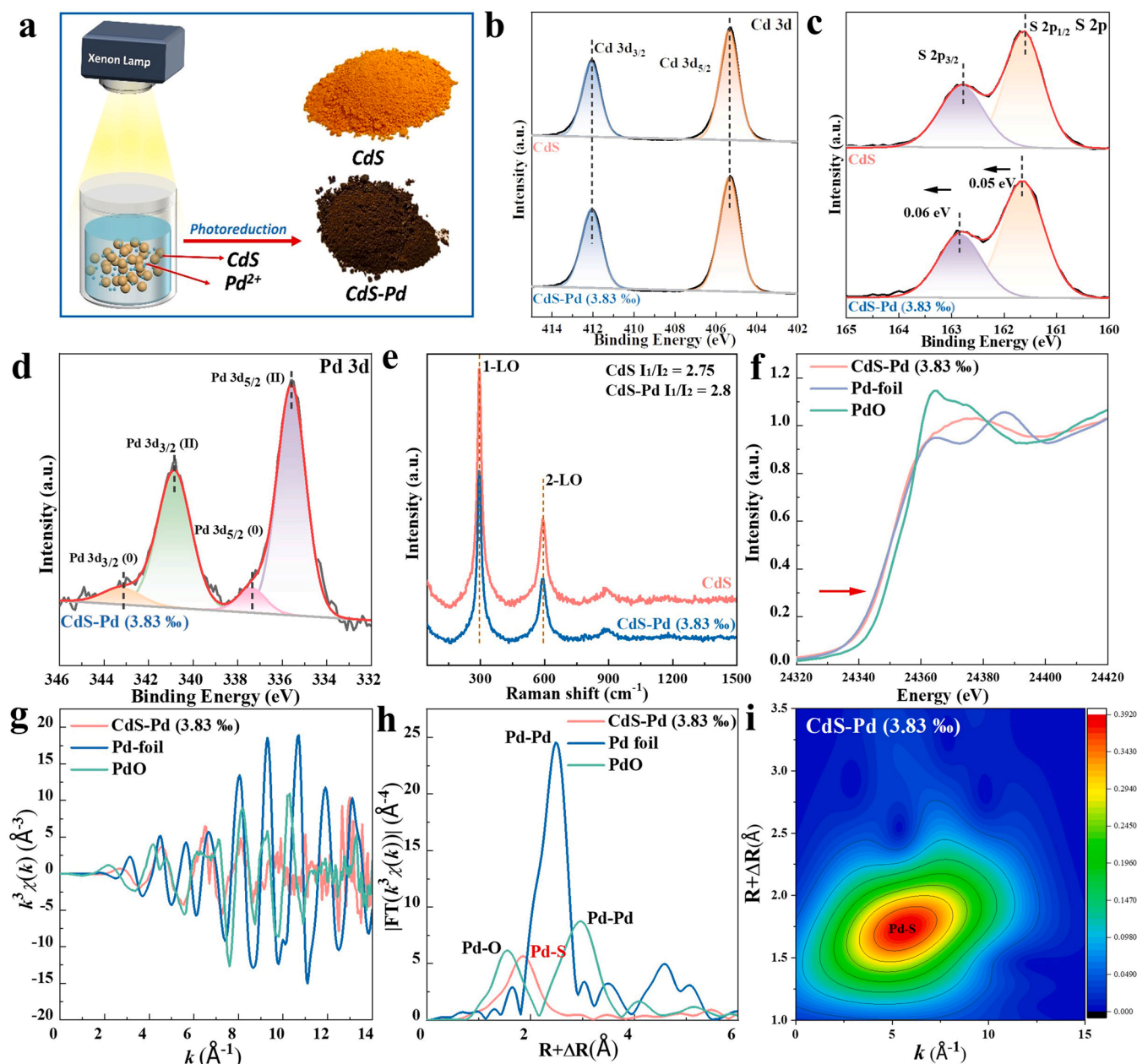


Fig. 1. (a) Preparation schematic diagram of CdS-Pd nanocatalyst. (b–d) XPS spectra and (e) Raman spectra of pure CdS NPs and CdS-Pd (3.83%) nanocatalyst. (f) XANES spectra, (g) k-space spectra and (h) EXAFS spectra of CdS-Pd (3.83%) nanocatalyst and reference samples (Pd foil and PdO). (i) Wavelet transform of CdS-Pd (3.83%) nanocatalyst, and the data of reference samples are shown in [Supplementary Material](#).

distribute on the surface of CdS as marked by red circles in Fig. 2c, which is further confirmed by the corresponding energy dispersive X-ray (EDX) mappings shown in Fig. 2e–g. Meanwhile, the selected area electron diffraction (SAED) of CdS-Pd (3.83%) nanocatalyst (Fig. 2d) shows the similar pattern with that of pure CdS NPs (Fig. 2b), further suggesting the ultra-low content of decorated Pd species on CdS NPs in a single-atomic state, which is consistent with XRD analysis (Fig. 1a). Moreover, the X-ray absorption fine structure (XAFS) of CdS-Pd (3.83%) nanocatalyst was studied. Fig. 1f shows that the X-ray absorption near-edge structure (XANES) spectrum of CdS-Pd (3.83%) nanocatalyst is very different from that of Pd foil and PdO, and its Pd K-edge locates at the right side of Pd foil (zero-valent state), indicating that its Pd element exists in positive-valent state. K-space spectra in Fig. 1g show that CdS-Pd (3.83%) nanocatalyst does not appear obvious signals of metal-metal bonding at high k value region, suggesting the single-atom state of Pd element in CdS-Pd (3.83%) nanocatalyst. Also, compared

with reference samples, its amplitude moves towards higher k value, indicating the formation of Pd-S coordination interaction. Furthermore, the signals assigned to elemental Pd and Pd cluster are not presented in the extended X-ray absorption fine structure (EXAFS) spectrum of CdS-Pd (3.83%) nanocatalyst (Fig. 1h), and only the signal assigned to Pd-S coordination can be observed, which further demonstrates the formation of strong coordination interaction between CdS NPs and Pd single-atoms. Its wavelet transform in Fig. 1i also supports this conclusion, and it is also consistent with XPS analysis.

3.2. Overall water splitting for hydrogen production

The SSL-induced HER activities of the nanocatalysts with different dosages of Pd SASS were evaluated, and the CdS-Pd (3.83%) nanocatalyst was confirmed to be the optimum catalyst for hydrogen production through overall water splitting (Fig. S1). Meanwhile, the pH

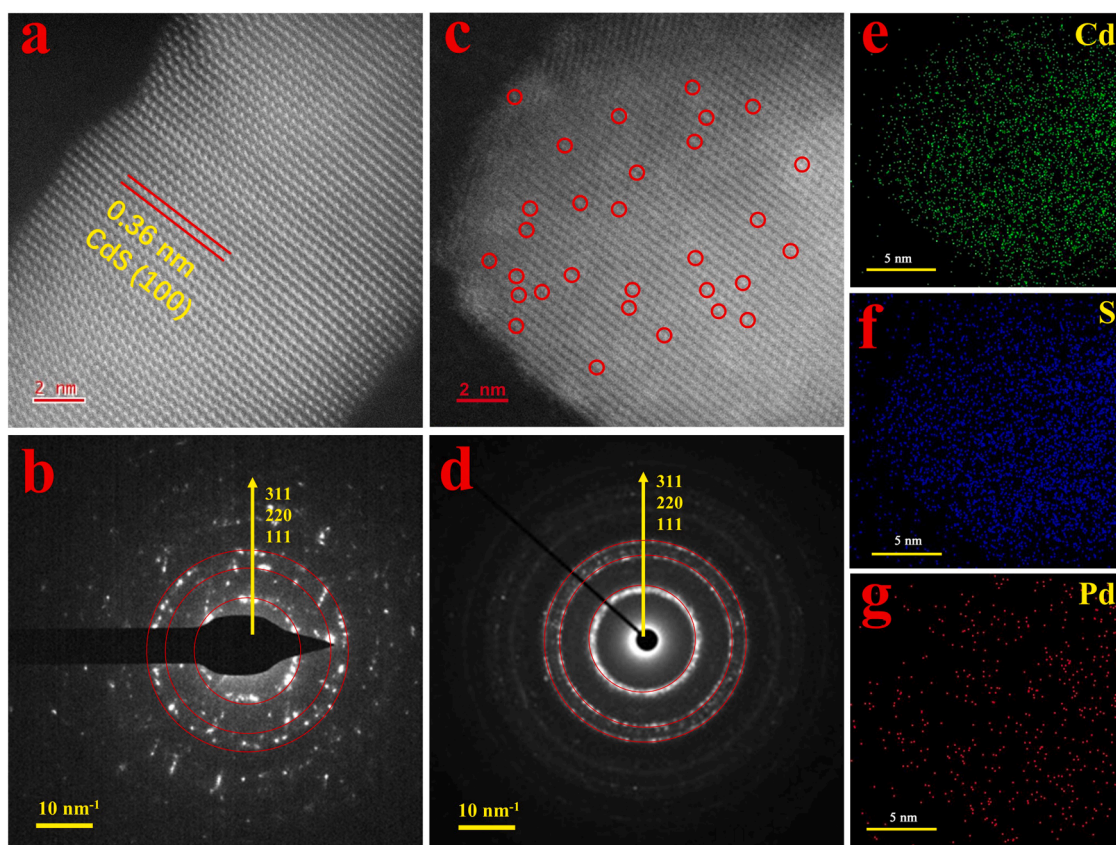


Fig. 2. AC HAADF-STEM images and SAED patterns of pure CdS NPs (a,b) and CdS-Pd (3.83%) nanocatalyst (c,d). (e–g) EDX mappings of CdS-Pd (3.83%) nanocatalyst.

value of 10 was confirmed to be the feasible pH condition for CdS-Pd (3.83%) nanocatalyst in overall water splitting (Fig. 3a). As shown in Fig. 3b, about 56.88 μmol hydrogen was evolved at 10 mg CdS-Pd (3.83%) nanocatalyst during 6 h (pH = 10), and its HER rate ($\sim 947.93 \mu\text{mol}\cdot\text{g}^{-1}\cdot\text{h}^{-1}$) is about 110-fold faster than that of pure CdS NPs ($\sim 8.64 \mu\text{mol}\cdot\text{g}^{-1}\cdot\text{h}^{-1}$). Comparatively, the HER performance of our optimum catalyst in overall water splitting is more prominent than other reported catalysts (Table 1) [37]. Furthermore, the AQYs of CdS-Pd (3.83%) nanocatalyst at different light wavelengths (420 nm, 500 nm, 550 nm and 600 nm) were tested and calculated according to the method in Supplementary Material. As displayed in Fig. 3f, when no scavenger is added into the reaction system, about 4.47% (420 nm), 1.81% (500 nm) and 0.52% (550 nm) of AQYs were achieved on CdS-Pd (3.83%) nanocatalyst. If TEOA is added into the reaction system, about 33.92% (420 nm), 27.49% (500 nm), 2.73% (550 nm) and 0.24% (600 nm) of AQYs were achieved on CdS-Pd (3.83%) nanocatalyst. The AQYs in both two reaction conditions are basically consistent with its UV–vis absorption spectrum, which further verifies high-efficient activity of CdS-Pd (3.83%) nanocatalyst under broadband light illumination. Meanwhile, the sample bottle containing the CdS-Pd (3.83%) nanocatalyst appears a large number of bubbles under outdoor sunlight irradiation (as shown in the inset of Fig. 3g). Therefore, it provides the visual evidence to demonstrate the high-efficiency of CdS-Pd (3.83%) nanocatalyst for hydrogen production under broadband light illumination. Also, the HER performance of CdS-Pd (3.83%) nanocatalyst was investigated in the presence of sacrificial agent (TEOA), and about 440.15 μmol hydrogen was evolved at 10 mg CdS-Pd (3.83%) nanocatalyst during 6 h (optimized pH value is 10.5, as Figs. S5 and 3c), and its HER rate ($\sim 8402.47 \mu\text{mol}\cdot\text{g}^{-1}\cdot\text{h}^{-1}$) is about 8.9-fold greater than overall water splitting performance and 25-fold greater than pure CdS NPs ($\sim 340.52 \mu\text{mol}\cdot\text{g}^{-1}\cdot\text{h}^{-1}$).

Moreover, the durability and reproducibility of CdS-Pd (3.83%) nanocatalyst were tested. As displayed in Fig. 3d, the CdS-Pd (3.83%) nanocatalyst presents not only remarkably enhanced HER activity but also the favorable linearity of the HER kinetic curve during 15 h of SSL-illumination, revealing the robust HER durability of CdS-Pd (3.83%) nanocatalyst in overall water splitting. Fig. 3e displays the cycling performance of CdS-Pd (3.83%) nanocatalyst in overall water splitting, and it presents unobvious HER activity variation during several cycling operations even being placed for several weeks in deionized water, suggesting the excellent reproducibility of CdS-Pd (3.83%) nanocatalyst in overall water splitting. Meanwhile, XPS spectra were recorded to investigate the structural stability of CdS-Pd (3.83%) nanocatalyst. Apparently, the characteristic peaks assigned to Cd $3d_{3/2}$ and Cd $3d_{5/2}$ orbitals of Cd^{2+} state are retained (Fig. S6a), but the characteristic peaks assigned to S^{2-} $2p_{3/2}$ (-0.07 eV), S^{2-} $2p_{1/2}$ (-0.06 eV), Pd^0 $3d_{3/2}$ (-1.85 eV), Pd^0 $3d_{5/2}$ (-1.28 eV), Pd^{2+} $3d_{3/2}$ (-1.02 eV) and Pd^{2+} $3d_{5/2}$ (-1.02 eV) orbitals appear slight shifts to lower binding energy (Figs. S6b and 3h), attributing to the slight influence to S-Pd bonding interaction after long-term photoirradiation. Besides, Fig. 3h shows the significantly increased electron density of Pd (0) chemical state compared with the fresh sample, reflecting further reduction of Pd species by photoinduced electrons during long-term photoirradiation, and this should be the main reason to affect the S-Pd bonding interaction. Therefore, it directly confirms that the photo-corrosion of CdS NPs can be highly restrained by Pd SASs decoration.

3.3. Optical and photo-electrochemical properties

UV–vis absorption spectra were measured to analyze the light-harvesting and optical-response properties of the catalysts. As shown in Fig. 4a, compared with pure CdS NPs, the CdS-Pd (3.83%)

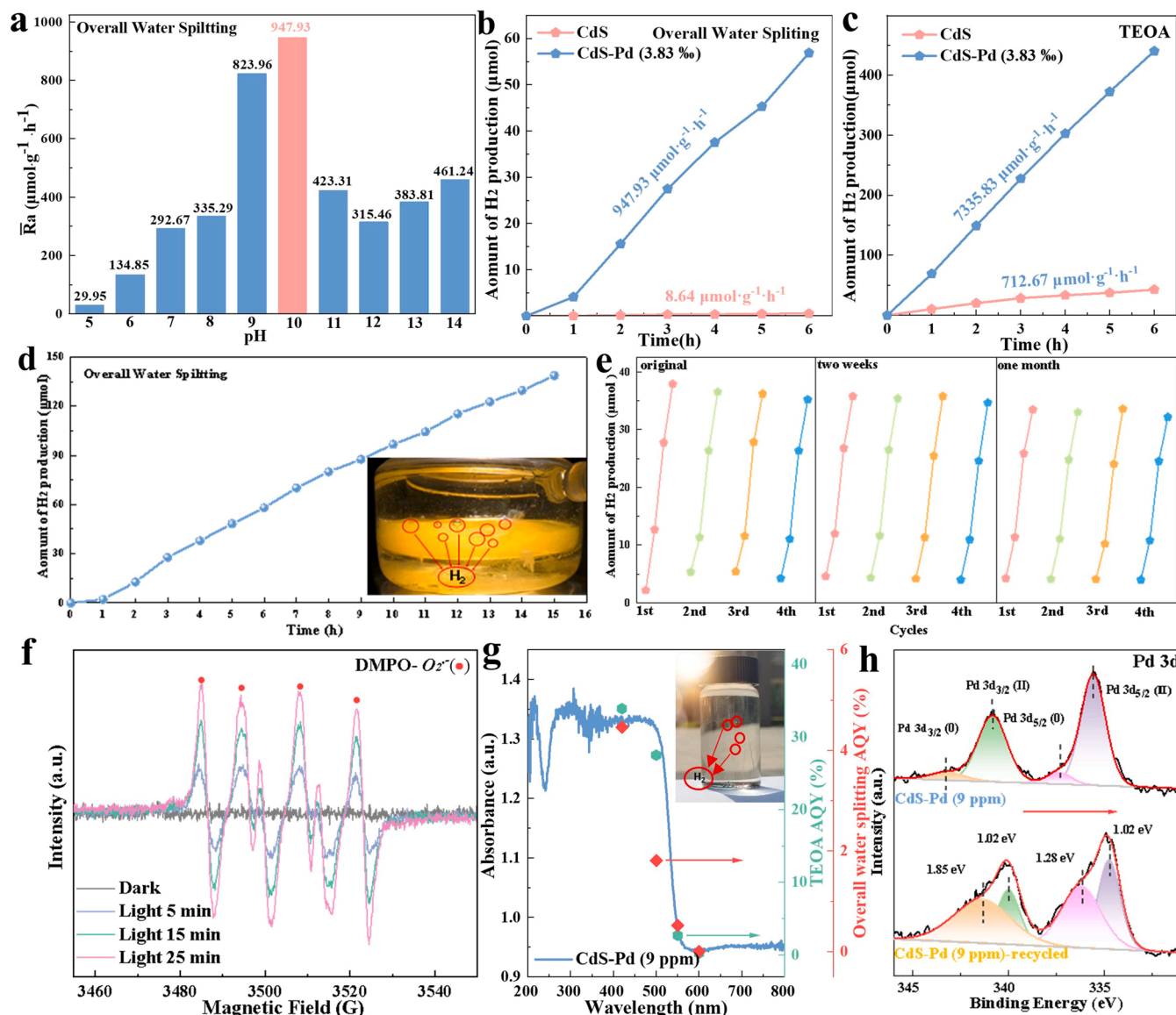


Fig. 3. (a) SSL-induced HER performances (different pH value), (d) durability, (e) reproducibility and (g) AQYs (420 nm, 500 nm, 550 nm and 600 nm) of CdS-Pd (3.83%) nanocatalyst at presence and absence of TEOA. HER kinetic curves of CdS NPs and CdS-Pd (3.83%) nanocatalyst in overall water splitting (b) and half water splitting (TEOA) (c). Pd 3d XPS spectra of fresh and recycled CdS-Pd (3.83%) nanocatalyst. (f) EPR spectra of CdS-Pd (3.83%) nanocatalyst aqueous dispersion during different illuminated time (0 min, 5 min, 15 min and 25 min) at the presence of scavenger (DMPO). The insets in panel d and g are the digital images of SSL-induced photoreactor (vacuum) and outdoor solar induced sample bottle (normal pressure) at the presence of CdS-Pd (3.83%) nanocatalyst.

nanocatalyst presents highly enhanced light-harvesting, and its maximum absorption edge red-shifts to 630 nm from 587 nm, suggesting that Pd SASs decoration remarkably improves the light-harvesting and optical-response properties of CdS NPs owing to the synergistic semiconductor (CdS)-metal (Pd) interaction. Furthermore, photoluminescence (PL) spectra were recorded to investigate the electron-hole recombination behavior of CdS-Pd (3.83%) nanocatalyst. Fig. 4b displays obvious emission peak at the range of 528–595 nm, and the peak intensity of CdS-Pd (3.83%) nanocatalyst weakens notably compared with that of pure CdS NPs, implying that electron-hole recombination is highly suppressed due to the synergistic CdS-to-Pd electron transfer. Also, the time-resolved transient decay PL spectra in Fig. 4c show that the CdS-Pd (3.83%) nanocatalyst presents conspicuously prolonged average lifetime ($\tau_A = 36,920$ ps) compared with pure CdS NPs ($\tau_A = 11,540$ ps), while more opportunities are available to induce water splitting for longer retention time of photoinduced carriers.

The electrochemical impedance spectroscopy (EIS) was performed to illustrate the interfacial resistance of the catalysts. As displayed in Fig. 4d, the CdS-Pd (3.83%) nanocatalyst presents smaller Nyquist arc than pure CdS NPs in dark, suggesting less interfacial resistance. When the ITO electrode was illuminated by xenon lamp (300 W), the Nyquist arc of CdS-Pd (3.83%) nanocatalyst was further reduced, but the pure CdS NPs presented enlarged Nyquist arc, indicating that the weak structural stability of pure CdS NPs and promoted interfacial conductivity of CdS-Pd (3.83%) nanocatalyst under photoirradiation. The charge separation properties of the catalysts under photoirradiation were explored by photocurrent measurement. As shown in Fig. 4e, pure CdS NPs presents stronger photocurrent response due to the low-work-function, but the response intensity decreases by about 45.77% during 520 s of illumination, attributing to the serious photocorrosion influence under long-term photoirradiation. Although the CdS-Pd (3.83%) nanocatalyst shows lower photocurrent intensity than pure CdS NPs, its response intensity keeps very stable under long-term photoirradiation,

Table 1

Comparison of photocatalytic HER performance with other reported photocatalysts.

Catalysts	Reaction condition				Performance		Refs.
	Solid content ^a	Light source	Scavenger	T ^b	HER rate	AQY	
Au-Pt-CdS	1.0 g/L	300 W Xe lamp ($\lambda > 420$ nm)	Na ₂ SO ₃ +Na ₂ S	RT	778 $\mu\text{mol}\cdot\text{h}^{-1}\cdot\text{g}^{-1}$	/	[34a]
TiO ₂ -Au-CdS	0.5 g/L	300 W Xe lamp ($\lambda > 420$ nm)	Na ₂ SO ₃ +Na ₂ S	RT	669.7 $\mu\text{mol}\cdot\text{h}^{-1}\cdot\text{g}^{-1}$	/	[34b]
CdS/Pt-N-TiO ₂	0.18 g/L	125 W Hg lamp ($\lambda > 290$ nm)	/	RT	639.2 $\mu\text{mol}\cdot\text{h}^{-1}\cdot\text{g}^{-1}$	/	[34c]
GaInZnON@-GaInON	0.75 g/L	300 W Xe lamp ($\lambda > 420$ nm)	/	RT	603 $\mu\text{mol}\cdot\text{h}^{-1}\cdot\text{g}^{-1}$	3.5% (430 nm)	[34d]
CdS/BCNNTs	0.1 g/L	300 W Xe lamp ($\lambda > 420$ nm)	/	6 °C	526.02 $\mu\text{mol}\cdot\text{h}^{-1}\cdot\text{g}^{-1}$	4.01% (420 nm)	[34e]
5% CoP/CdS-P	0.25 g/L	LED light source (30 × 3 W, $\lambda > 420$ nm)	/	RT	231 $\mu\text{mol}\cdot\text{h}^{-1}\cdot\text{g}^{-1}$	/	[34f]
CdS/NiOOH	0.13 g/L	300 W Xe lamp ($\lambda > 420$ nm)	/	RT	118.6 $\mu\text{mol}\cdot\text{h}^{-1}\cdot\text{g}^{-1}$	3.67% (420 nm)	[34g]
CDs-CdS	2 g/L	300 W Xe lamp ($\lambda > 420$ nm)	/	25 °C	51 $\mu\text{mol}\cdot\text{h}^{-1}\cdot\text{g}^{-1}$	/	[34h]
TJU-16-Rh _{0.22}	1 g/L	AM 1.5 G SSL	/	RT	31 $\mu\text{mol}\cdot\text{h}^{-1}\cdot\text{g}^{-1}$	/	[34i]
TiO ₂ /CdS+Pt	0.67 g/L	300 W Xe lamp ($\lambda > 420$ nm)	/	RT	3.074 $\mu\text{mol}\cdot\text{h}^{-1}\cdot\text{g}^{-1}$	0.17% (430 nm)	[34j]
CdS-Pd (3.83%)	0.2 g/L	300 W Xe lamp	/	5 °C	947.9 $\mu\text{mol}\cdot\text{h}^{-1}\cdot\text{g}^{-1}$	4.47% (420 nm)	This work
					8.4 $\mu\text{mol}\cdot\text{h}^{-1}\cdot\text{g}^{-1}$	33.9% (420 nm)	
					mmol·h ⁻¹ ·g ⁻¹	(420 nm)	

^a Solid content means catalyst concentration in reaction system.^b T is reaction temperature.

attributing to the effective restraining effect on the photocorrosion of CdS NPs due to the promoted CdS-to-Pd electron transfer. This conclusion is consistent with the results of PL and EIS analysis. Also, linear cyclic voltammetry (LSV) curves were tested under chopped-illumination to further investigate the photo-electrochemical properties of the catalysts. Fig. 4f shows that the CdS-Pd (3.83%) nanocatalyst displays more stable photocurrent response than pure CdS NPs during wide onset potential range, which further demonstrates the excellent photo-electrochemical stability of CdS-Pd (3.83%) nanocatalyst. Besides, to verify the effective restraining to the photocorrosion of CdS NPs by Pd SAs decoration, Tafel polarization curves were recorded in dark and under illumination. As shown in Fig. 4g, the CdS-Pd (3.83%) nanocatalyst presents larger polarized overpotential ($\eta = 1013$ mV) than pure CdS NPs ($\eta = 977$ V) in dark, but the opposite result ($\eta_{\text{CdS-Pd}}$ (992 mV) $< \eta_{\text{CdS}}$ (1045 mV)) is obtained under photoirradiation, suggesting the enhanced photoelectric reduction ability of CdS-Pd (3.83%) nanocatalyst. Additionally, Mott-Schottky measurements were conducted to further confirm the electron transfer direction of CdS-Pd (3.83%) nanocatalyst (Fig. S7), and the linear part of CdS-Pd (3.83%) nanocatalyst possesses larger slope than pure CdS NPs, suggesting the formation of promoted CdS-to-Pd electron transfer.

3.4. CdS-to-Pd electron transfer mechanism for water splitting

To clarify the band structure of CdS-Pd (3.83%) nanocatalyst, the valence band maximum (VBM) vs. Fermi level ($|E_{\text{VB}}-E_{\text{F}}|$) of pure CdS NPs is confirmed to be ~ 1.65 eV from its XPS-VBM spectrum in Fig. S8, and its bandgap (E_{g}) is determined to be ~ 2.22 eV from its $(\alpha h\nu)^{1/2}$ - $h\nu$ pattern (Fig. S9) obtained according to the Kubelka-Munk function in Supplementary Material [38]. Thus, the conduction band (CB) position vs. E_{F} is derived to be ~ -0.57 eV according to the formula of $E_{\text{g}} = E_{\text{VB}} - E_{\text{CB}}$ [39]. After Pd SAs decoration, the CdS-Pd (3.83%) nanocatalyst is easier to be excited under broadband light, and the photoinduced electrons on the CB position of CdS can rapidly transfer to surface Pd SAs due to the synergetic semiconductor (CdS)-metal (Pd) interaction (as part (I) in Fig. 4h) [40]. Because Pd SAs are only decorated on the outer surface of CdS NPs, the photoinduced electrons can quickly migrate to the surface Pd sites from the bulk phase of CdS NPs (as part

(II) in Fig. 4h), which highly restrains the recombination of photoinduced carriers and achieves high-efficient hydrogen production on surface Pd SAs under SSL-irradiation. Additionally, the gas chromatograph (GC) analysis in Fig. S10b demonstrates the synchronous evolution of hydrogen and oxygen on CdS-Pd (3.83%) nanocatalyst, but only the peak areas of hydrogen increase linearly as time prolongs. Electron paramagnetic resonance (EPR) spectra in Fig. 3f indicate the generation of superoxide ($\text{O}_2^{\cdot-}$) radicals, and its characteristic signals present increasing intensity as illuminated time prolongs (0, 5, 15 and 25 min), suggesting further reaction between O_2 molecules and photoinduced electrons. Therefore, it reveals that the CdS-Pd (3.83%) nanocatalyst is more suitable for hydrogen production in overall water splitting.

3.5. DFT analysis

According to the results of AC HAADF-STEM analysis in Fig. 2, the (100) plane of CdS NPs was confirmed as the main crystal plane to anchor the Pd SAs, and the optimized configurations of CdS NPs and CdS-Pd nanocatalyst are given as model 1 (CdS) and model 2 (CdS-Pd) based on the (100) plane of CdS (Fig. 5a). The electron transfer mode of the CdS-Pd nanocatalyst was further analyzed by density functional theory (DFT) calculations. The total density of states (TDOS) show that model 2 displays lower TDOS intensity than model 1 (Fig. 5d), further verifying the formation of CdS-to-Pd electron transfer. Especially, all electron orbitals of S atom display remarkably reduced partial DOS (PDOS) after Pd SAs decoration (Figs. 5e and S11), and the hybridization between the electron orbitals of S atom and Pd atom can be observed from their PDOS, which also confirms the formation of S-Pd bonding interaction and well explains the reason for lower photocurrent intensity of CdS-Pd (3.83%) nanocatalyst than pure CdS NPs (Fig. 3e). Furthermore, water splitting process is the rate controlling step of HER, thus its energy barriers on two models were calculated as Fig. 5b. The model 2 displays smaller activation barrier (0.93 eV) than model 1 (1.31 eV), suggesting easier water splitting on CdS-Pd nanocatalyst. Meanwhile, the Gibbs free energy changes of H^* intermediate adsorption (ΔG_{H^*}) on two models were also calculated. According to Sabatier principle, excellent HER activity may be presented when ΔG_{H^*} closes to zero [41]. As shown in Fig. 5c, Cd atom of model 1 possesses large energy barrier (1.94 eV), but

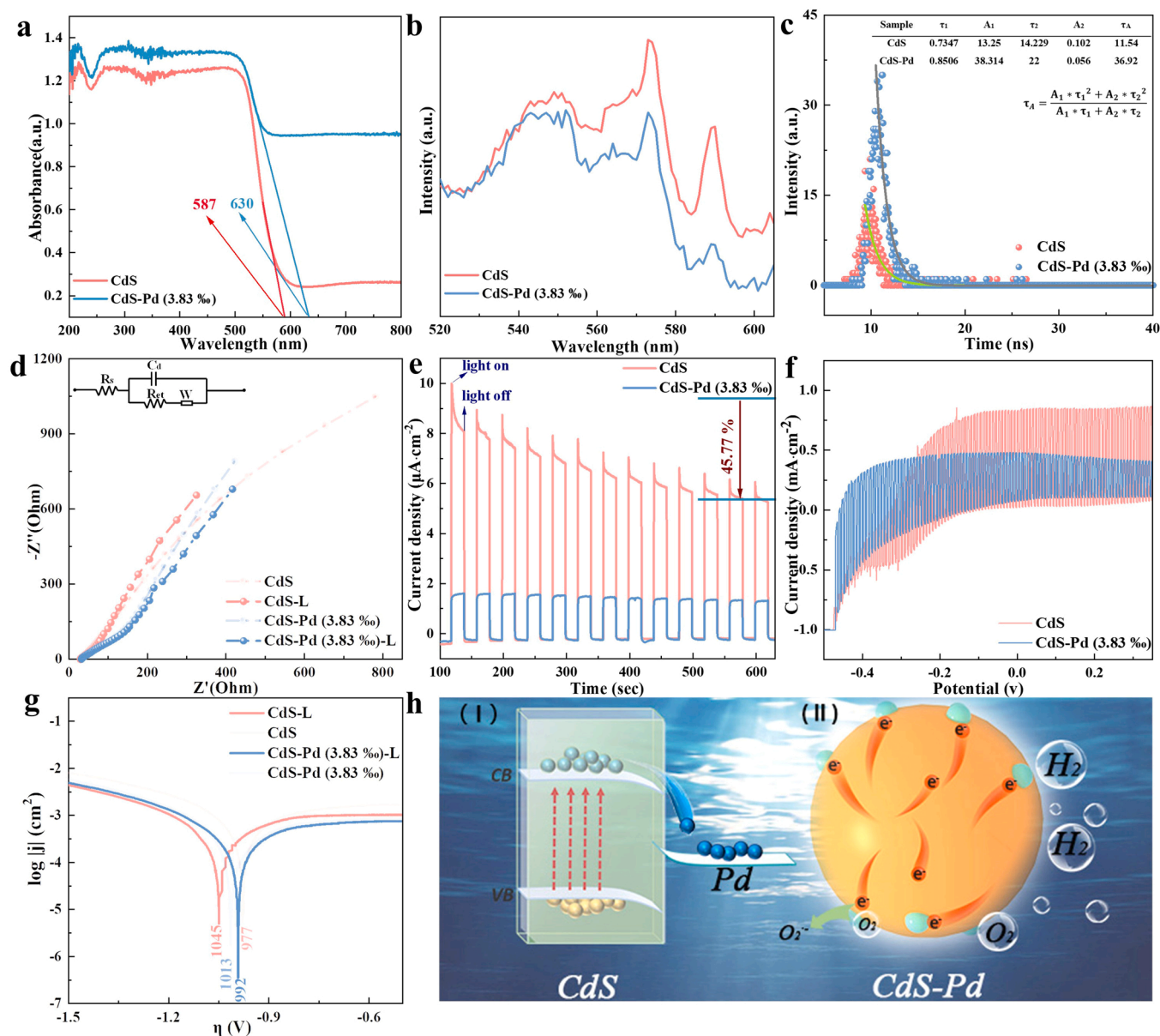


Fig. 4. (a) UV-vis absorption spectra, (b) PL spectra, (c) TRPL spectra, (d) EIS curves (dark and light), (e) transient photocurrent responses, (f) LSV curves (under chopped-illumination) and (g) Tafel curves (dark and light) of pure CdS NPs and CdS-Pd (3.83%) nanocatalyst. (h) CdS-to-Pd electron transfer mechanism of CdS-Pd (3.83%) nanocatalyst in overall water splitting.

its S atom displays much smaller energy barrier (0.59 eV), revealing that S atom of model 1 is the main reactive site for HER. After Pd SASs decoration, the energy barrier of S atom (0.14 eV) is further reduced, and the Pd atom also displays much smaller energy barrier (0.36 eV) than S atom (0.59 eV) in model 1. Considering that Pd atom only exists on the outer surface of CdS NPs in the actual situation, thereby S atom and Pd atom in model 2 synergistically serve as the reactive sites for hydrogen production. Therefore, the overall reaction mechanism can be proposed as Fig. 5f. Briefly, water molecules are firstly adsorbed on the surface of CdS-Pd nanocatalyst (step 1), then its O-H bonds were weakened (step 2) and broken (step 3) on Pd atom sites to form the H^* intermediates and OH^- ions. The H^* intermediates can be easily converted into hydrogen after accepting electrons due to the fast S-to-Pd electron transfer (step 4), and the OH^- ions will convert into oxygen when further reacting with photogenerated holes (step 5). Because of the side reaction ($O_2 + e^- \rightarrow O_2^-$), this catalyst is more suitable for hydrogen production in overall water splitting. This result is consistent with what concluded from experimental studies.

4. Conclusion

In this study, to suppress the influence of photocorrosion on CdS microstructure under long-term photoreaction, a Pd SASs decorated CdS (CdS-Pd) nanocatalyst was synthesized via a simple and controllable photoinduced reduction strategy. Experimental results suggest that fast bulk-to-surface electron migration is achieved due to the synergistic semiconductor (CdS)-metal (Pd) interaction, thereby the resultant CdS-Pd (3.83%) nanocatalyst shows considerable structural stability and about 110-fold greater solar-induced HER activity compared to pure CdS NPs in overall water splitting. Meanwhile, high AQYs of 4.47%/1.81% and 33.92%/27.49% were respectively achieved on the decorated CdS nanocatalyst under the light of 420 nm/500 nm in absence and presence of scavenger, which also demonstrates its high-efficiency under broadband light irradiation. DFT calculations further explain the internal mechanism of promoted hydrogen production on CdS-Pd (3.83%) nanocatalyst based on water splitting energy barriers and HER energy barriers. The present work provides an important insight into gaining

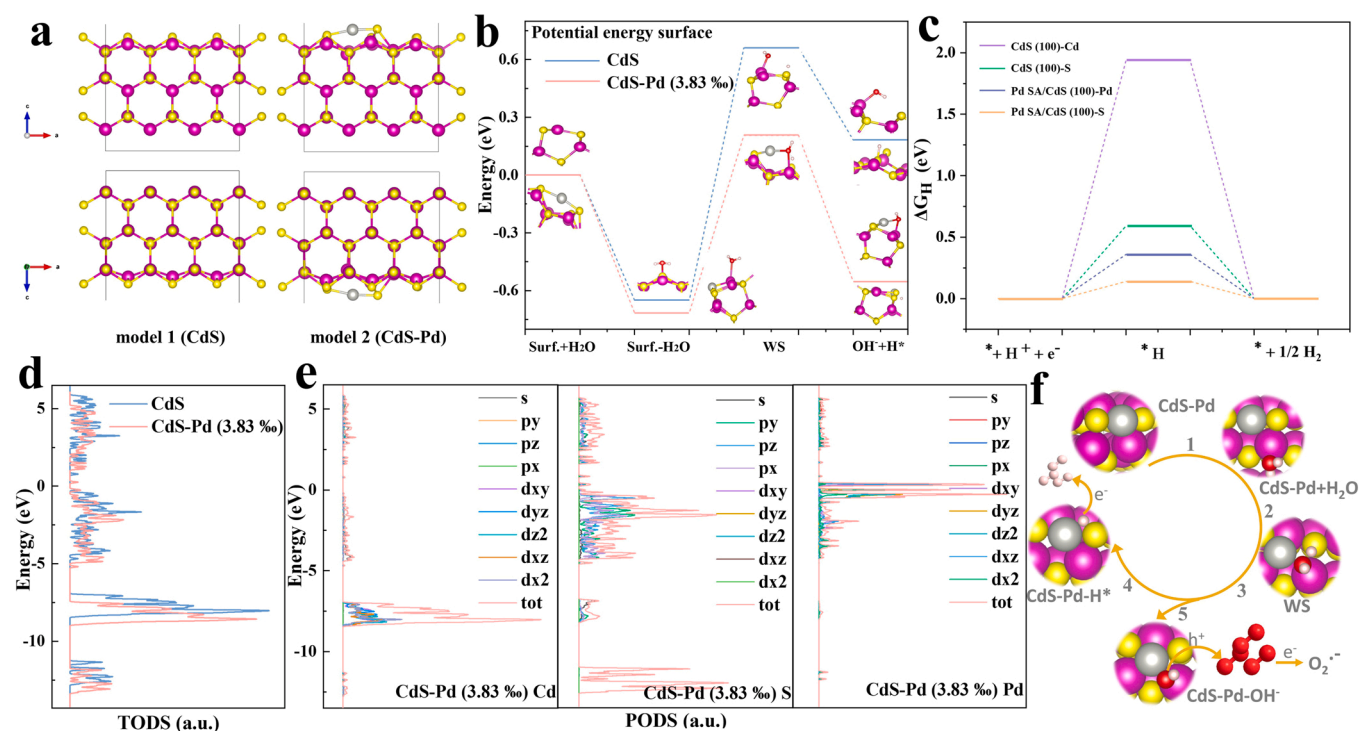


Fig. 5. (a) Optimized configurations, (b) water splitting energy barriers and (c) HER energy barriers of model 1 (CdS) and model 2 (CdS-Pd nanocatalyst). (d) DOS and (e) catalytic mechanism of model 2 (CdS-Pd nanocatalyst). All the computational results were calculated based on the (100) plane of CdS.

stable CdS-based photocatalyst for high-efficient hydrogen production by overall water splitting.

CRediT authorship contribution statement

No conflict of interest exists in the submission of this manuscript, and manuscript is approved by all authors for publication., **Wei Li**: Data curation, Project administration, Resources, Methodology, Supervision, Validation, Writing – original draft, Writing – review & editing. **Xiao-shan Chu**: Investigation, Writing – original draft, Writing – review & editing. **Fei Wang**: Investigation. **Yan-yan Dang**: Investigation. **Xiao-yun Liu**: Investigation. **Teng-hao Ma**: Investigation. **Jia-yuan Li**: Investigation. **Chuan-yi Wang**: Resources, Methodology, Supervision, Validation.

Declaration of Competing Interest

The authors declare no competing financial interests.

Acknowledgements

The authors are grateful for the financial supports of the National Natural Science Foundation of China (21806098) and Basic Research Fund of Shaanxi University of Science & Technology (2016GBJ-22). The X-ray absorption spectra (XAS) including X-ray absorption near-edge structure (XANES) and extended X-ray absorption fine structure (EXAFS) of the sample at K-edge was collected at the Beamline of TPS44A1 in National Synchrotron Radiation Research Center (NSRRC), Taiwan.

Appendix A. Supporting information

Supplementary data associated with this article can be found in the online version at [doi:10.1016/j.apcatb.2021.121000](https://doi.org/10.1016/j.apcatb.2021.121000).

References

- [1] a) C.-C. Hou, H.-F. Wang, C. Lia, Q. Xu, From metal–organic frameworks to single/dual-atom and cluster metal catalysts for energy applications, *Energy Environ. Sci.* 13 (2020) 1658–1693; b) I. Jang, K. Im, H. Shin, K.-S. Lee, H. Kim, J. Kim, S.J. Yoo, Electron-deficient titanium single-atom electrocatalyst for stable and efficient hydrogen production, *Nano Energy* 78 (2020), 105151.
- [2] a) Q. Zhang, J. Guan, Recent progress in single-atom catalysts for photocatalytic water splitting, *Sol. RRL* 4 (2020), 2000283; b) H. Luo, Y. Liu, S.D. Dimitrov, L. Steier, S. Guo, X. Li, J. Feng, F. Xie, Y. Fang, A. Sapelkin, X. Wang, M.-M. Titirici, Pt single-atoms supported on nitrogen-doped carbon dots for highly efficient photocatalytic hydrogen generation, *J. Mater. Chem. A* 8 (2020) 14690–2014696.
- [3] a) D.W. Wakerley, M.F. Kuehnle, K.L. Orchard, K.H. Ly, T.E. Rosser, E. Reisner, Solar-driven reforming of lignocellulose to H₂ with a CdS/CdOx photocatalyst, *Nat. Energy* 2 (2017) 17021; b) G. Liu, C. Kolodziej, R. Jin, S. Qi, Y. Lou, J. Chen, D. Jiang, Y. Zhao, C. Burda, MoS₂-stratified CdS-Cu₂xS core-shell nanorods for highly efficient photocatalytic hydrogen production, *ACS Nano* 14 (2020) 5468–5479.
- [4] J. Sobhanan, P. Jones, R. Kohara, S. Sugino, M. Vacha, C. Subrahmanyam, Y. Takano, F. Lacy, V. Biju, Toxicity of nanomaterials due to photochemical degradation and the release of heavy metal ions, *Nanoscale* 12 (2020) 22049–22058.
- [5] a) X. Li, L. Liu, X. Ren, J. Gao, Y. Huang, B. Liu, *Sci. Adv.* 6 (2020), eabb6833; b) Y. Wang, Y. Liu, W. Liu, J. Wu, Q. Li, Q. Feng, Z. Chen, X. Xiong, D. Wang, Y. Lei, Regulating the coordination structure of metal single atoms for efficient electrocatalytic CO₂ reduction, *Energy Environ. Sci.* 13 (2020) 4609–4624.
- [6] J.N. Tiwari, N.K. Dang, H.J. Park, S. Sultan, M.G. Kim, J. Haiyan, Z. Lee, K.S. Kim, Remarkably enhanced catalytic activity by the synergistic effect of palladium single atoms and palladium–cobalt phosphide nanoparticles, *Nano Energy* 78 (2020), 105166.
- [7] Q. Wang, X. Huang, Z.L. Zhao, M. Wang, B. Xiang, J. Li, Z. Feng, H. Xu, M. Gu, Ultrahigh-loading of Ir single atoms on NiO matrix to dramatically enhance oxygen evolution reaction, *J. Am. Chem. Soc.* 142 (2020) 7425–7433.
- [8] B.-H. Lee, S. Park, M. Kim, A.K. Sinha, S.C. Lee, E. Jung, W.J. Chang, K.-S. Lee, J. H. Kim, S.-P. Cho, H. Kim, K.T. Nam, T. Hyeon, Reversible and cooperative photoactivation of single-atom Cu/TiO₂ photocatalysts, *Nat. Mater.* 18 (2019) 620–626.
- [9] a) Y. Chen, S. Ji, W. Sun, Y. Lei, Q. Wang, A. Li, W. Chen, G. Zhou, Z. Zhang, Y. Wang, L. Zheng, Q. Zhang, L. Gu, X. Han, D. Wang, Y. Li, Engineering the atomic interface with single platinum atoms for enhanced photocatalytic hydrogen production, *Angew. Chem. Int. Ed.* 59 (2020) 1295–1301; b) M. Yoo, Y.-S. Yu, H. Ha, S. Lee, J.-S. Choi, S. Oh, E. Kang, H. Choi, H. An, K.-S. Lee, J.Y. Park, R. Celestre, M.A. Marcus, K. Nowrouzi, D. Taube, D.A. Shapiro, W. Jung, C. Kim, H.Y. Kim, CT and MR imaging findings of ocular adnexal mucosa-

- associated lymphoid tissue lymphoma associated with IgG₄-related disease: multi-institutional case series, *Energy Environ. Sci.* 13 (2020) 1231–1239.
- [10] T. Wang, X. Tao, X. Li, K. Zhang, S. Liu, B. Li, Synergistic Pd single atoms, clusters, and oxygen vacancies on TiO₂ for photocatalytic hydrogen evolution coupled with selective organic oxidation, *Small* 17 (2021), 2006255.
 - [11] R. Feng, K. Wan, X. Sui, N. Zhao, H. Li, W. Lei, J. Yu, X. Liu, X. Shi, M. Zhai, G. Liu, H. Wang, L. Zheng, M. Liu, Anchoring single Pt atoms and black phosphorene dual co-catalysts on CdS nanospheres to boost visible-light photocatalytic H₂ evolution, *Nano Today* 37 (2021), 101080.
 - [12] S. Cai, M. Zhang, J. Li, J. Chen, H. Jia, Anchoring single-atom Ru on CdS with enhanced CO₂ capture and charge accumulation for high selectivity of photothermocatalytic CO₂ reduction to solar fuels, *Sol. RRL* 5 (2021), 2000313.
 - [13] P. Zhou, Q. Zhang, Y. Chao, L. Wang, Y. Li, H. Chen, L. Gu, S. Guo, Exonuclease 1 (EXO1) is a potential prognostic biomarker and correlates with immune infiltrates in lung adenocarcinoma, *Chem* 7 (2021) 1033–1049.
 - [14] Y. Cao, L. Guo, M. Dan, D.E. Doronkin, C. Han, Z. Rao, Y. Liu, J. Meng, Z. Huang, K. Zheng, P. Chen, F. Dong, Y. Zhou, Modulating electron density of vacancy site by single Au atom for effective CO₂ photoreduction, *Nat. Commun.* 12 (2021) 1675.
 - [15] a) W. Zhang, Q. Peng, L. Shi, Q. Yao, X. Wang, A. Yu, Z. Chen, Y. Fu, Merging single-atom-dispersed iron and graphitic carbon nitride to a joint electronic system for high-efficiency photocatalytic hydrogen evolution, *Small* 15 (2019) 1905166; b) Y. Gao, Y. Zhu, T. Li, Z. Chen, Q. Jiang, Z. Zhao, X. Liang, C. Hu, Unraveling the high-activity origin of single-atom iron catalysts for organic pollutant oxidation via peroxymonosulfate activation, *Environ. Sci. Technol.* 55 (2021) 8318–1908328.
 - [16] X. Jin, R. Wang, L. Zhang, R. Si, M. Shen, M. Wang, J. Tian, J. Shi, Electron configuration modulation of nickel single atoms for elevated photocatalytic hydrogen evolution, *Angew. Chem. Int. Ed.* 59 (2020) 6827–6831.
 - [17] X. Xiao, Y. Gao, L. Zhang, J. Zhang, Q. Zhang, Q. Li, H. Bao, J. Zhou, S. Miao, N. Chen, J. Wang, B. Jiang, C. Tian, H. Fu, A promoted charge separation/transfer system from Cu single atoms and C₃N₄ layers for efficient photocatalysis, *Adv. Mater.* 32 (2020), 2003082.
 - [18] X.-H. Jiang, L.-S. Zhang, H.-Y. Liu, D.-S. Wu, F.-Y. Wu, L. Tian, L.-L. Liu, J.-P. Zou, S.-L. Luo, B.-B. Chen, Silver single atom in carbon nitride catalyst for highly efficient photocatalytic hydrogen evolution, *Angew. Chem. Int. Ed.* 59 (2020) 23112–23116.
 - [19] L. Zeng, C. Dai, B. Liu, C. Xue, Oxygen-assisted stabilization of single-atom Au during photocatalytic hydrogen evolution, *J. Mater. Chem. A* 7 (2019) 24217–24221.
 - [20] L. Zhang, R. Long, Y. Zhang, D. Duan, Y. Xiong, Y. Zhang, Y. Bi, Direct observation of dynamic bond evolution in single-atom Pt/C₃N₄ catalysts, *Angew. Chem. Int. Ed.* 132 (2020) 6283–6288.
 - [21] G. Liu, Y. Huang, H. Lv, H. Wang, Y. Zeng, M. Yuan, Q. Meng, C. Wang, Confining single-atom Pd on g-C₃N₄ with carbon vacancies towards enhanced photocatalytic NO conversion, *Appl. Catal. B Environ.* 284 (2021), 119683.
 - [22] J.-H. Zhang, W. Yang, M. Zhang, H.-J. Wang, R. Si, D.-C. Zhong, T.-B. Lu, Metal-organic layers as a platform for developing single-atom catalysts for photochemical CO₂ reduction, *Nano Energy* 80 (2021), 105542.
 - [23] R. Shi, C. Tian, X. Zhu, C.-Y. Peng, B. Mei, L. He, X.-L. Du, Z. Jiang, Y. Chen, S. Dai, Achieving an exceptionally high loading of isolated cobalt single atoms on a porous carbon matrix for efficient visible-light-driven photocatalytic hydrogen production, *Chem. Sci.* 10 (2019) 2585–2591.
 - [24] Q. Zuo, T. Liu, C. Chen, Y. Ji, X. Gong, Y. Mai, Y. Zhou, Ultrathin metal-organic framework nanosheets with ultrahigh loading of single Pt atoms for efficient visible-light-driven photocatalytic H₂ evolution, *Angew. Chem. Int. Ed.* 58 (2019) 10198–10203.
 - [25] G. Wang, C.-T. He, R. Huang, J. Mao, D. Wang, Y. Li, Photoinduction of Cu single atoms decorated on UiO-66-NH₂ for enhanced photocatalytic reduction of CO₂ to liquid fuels, *J. Am. Chem. Soc.* 142 (2020) 19339–19345.
 - [26] P. Huang, M. Cheng, H. Zhang, M. Zuo, C. Xiao, Y. Xie, Single Mo atom realized enhanced CO₂ electro-reduction into formate on N-doped graphene, *Nano Energy* 61 (2019) 428–434.
 - [27] M. Sun, J. Ji, M. Hu, M. Weng, Y. Zhang, H. Yu, J. Tang, J. Zheng, Z. Jiang, F. Pan, C. Liang, Z. Lin, Overwhelming the performance of single atoms with atomic clusters for platinum-catalyzed hydrogen evolution, *ACS Catal.* 9 (2019) 8213–8223.
 - [28] a) B. Han, Y. Guo, Y. Huang, W. Xi, J. Xu, J. Luo, H. Qi, Y. Ren, X. Liu, B. Qiao, T. Zhang, Strong metal-support interactions between Pt single atoms and TiO₂, *Angew. Chem. Int. Ed.* 59 (2020) 11824–11829; b) J. Xi, H.S. Jung, Y. Xu, F. Xiao, J.W. Bae, S. Wang, Synthesis strategies, catalytic applications, and performance regulation of single-atom catalysts, *Adv. Funct. Mater.* 31 (2021) 2008318; c) H.-Y. Zhuo, X. Zhang, J.-X. Liang, Q. Yu, H. Xiao, J. Li, Theoretical understandings of graphene-based metal single-atom catalysts: stability and catalytic performance, *Chem. Rev.* 120 (2020) 12315–12341.
 - [29] a) J. Wang, L. Xu, T. Wang, R. Li, Y. Zhang, J. Zhang, T. Peng, *Adv. Funct. Mater.* 11 (2021), 2003575; b) D. Zhao, Y. Wang, C.-L. Dong, Y.-C. Huang, J. Chen, F. Xue, S. Shen, L. Guo, Boron-doped nitrogen-enriched carbon nitride-based Z-scheme heterostructures for photocatalytic overall water splitting, *Nat. Energy* 6 (2021) 388–397; c) F. Zhang, Y. Zhu, Q. Lin, L. Zhang, X. Zhang, H. Wang, Pyromellitic-based low molecular weight gelators and computational studies of intermolecular interactions: a potential additive for lubricant, *Energy Environ. Sci.* 14 (2021) 2954–3009.
 - [30] a) W. Li, X. Wang, Q. Ma, F. Wang, X. Chu, X. Wang, C. Wang, CdS@h-BN heterointerface construction on reduced graphene oxide nanosheets for hydrogen production, *Appl. Catal. B Environ.* 284 (2021), 119688; b) W. Li, Q. Ma, X. Wang, X. Chu, F. Wang, X. Wang, C. Wang, Enhanced photoresponse and fast charge transfer: three-dimensional macroporous g-C₃N₄/GO-TiO₂ nanostructure for hydrogen evolution, *J. Mater. Chem. A* 8 (2020) 19533–19543.
 - [31] R. Gao, J. Wang, Z.-F. Huang, R. Zhang, W. Wang, L. Pan, J. Zhang, W. Zhu, X. Zhang, C. Shi, J. Lim, Ji-Jun Zou, Pt/Fe₂O₃ with Pt-Fe pair sites as a catalyst for oxygen reduction with ultralow Pt loading, *Nat. Energy* 6 (2021) 614–623.
 - [32] a) Y. Wu, X. Chen, J. Cao, Y. Zhu, W. Yuan, Z. Hu, Z. Ao, G.W. Brudvig, F. Tian, J. C. Yu, C. Li, Photocatalytically recovering hydrogen energy from wastewater treatment using MoS₂@TiO₂ with sulfur/oxygen dual-defect, *Appl. Catal. B Environ.* 303 (2022), 120878; b) J. Liu, X. Liu, H. Shi, J. Luo, L. Wang, J. Liang, S. Li, L.-M. Yang, T. Wang, Y. Huang, Q. Li, Breaking the scaling relations of oxygen evolution reaction on amorphous NiFeP nanostructures with enhanced activity for overall seawater splitting, *Appl. Catal. B Environ.* 302 (2022), 120862.
 - [33] H. Chen, W. Liu, A. Laemont, C. Krishnaraj, X. Feng, F. Rohman, M. Meledina, Q. Zhang, R.V. Deun, K. Leus, P.V.D. Voort, A visible-light-harvesting covalent organic framework bearing single nickel sites as a highly efficient sulfur-carbon cross-coupling dual catalyst, *Angew. Chem. Int. Ed.* 60 (2021) 10820–10827.
 - [34] Y.-X. Tan, Z.-M. Chai, B.-H. Wang, S. Tian, X.-X. Deng, Z.-J. Bai, L. Chen, S. Shen, J.-K. Guo, M.-Q. Cai, C.-T. Au, S.-F. Yin, Boosted Photocatalytic oxidation of toluene into benzaldehyde on CdIn₂S₄-CdS: synergistic effect of compact heterojunction and S-vacancy, *ACS Catal.* 11 (2021) 2492–2503.
 - [35] L. Zhao, T. Dong, J. Du, H. Liu, H. Yuan, Y. Wang, J. Jia, H. Liu, W. Zhou, Synthesis of CdS/MoS₂ nanooctahedrons heterostructure with a tight interface for enhanced photocatalytic H₂ evolution and biomass upgrading, *Sol. RRL* 5 (2021), 2000415.
 - [36] Y. Kim, Z. Hu, I.D. Avdeev, A. Singh, A. Singh, V. Chandrasekaran, M.O. Nestoklon, S.V. Goupalov, J.A. Hollingsworth, H. Htoon, Interplay of bright triplet and dark excitons revealed by magneto-photoluminescence of individual PbS/CdS quantum dots, *Small* 17 (2021), 2006977.
 - [37] a) L. Ma, K. Chen, F. Nan, J. Wang, D. Yang, L. Zhou, Q. Wang, Improved hydrogen production of Au-Pt-CdS hetero-nanostructures by efficient plasmon-induced multipathway electron transfer, *Adv. Funct. Mater.* 26 (2016) 6076–6083; b) X. Yao, X. Hu, W. Zhang, X. Gong, X. Wang, S.C. Pillai, D.D. Dionysiou, D. Wang, Mie resonance in hollow nanoshells of ternary TiO₂-Au-CdS and enhanced photocatalytic hydrogen evolution, *Appl. Catal. B Environ.* 276 (2020), 119153; c) M. Solakidou, A. Giannakas, Y. Georgiou, N. Boukos, M. Louloudi, Y. Deligiannakis, Efficient photocatalytic water-splitting performance by ternary CdS/Pt-N-TiO₂ and CdS/Pt-N,F-TiO₂: interplay between CdS photo corrosion and TiO₂-doping, *Appl. Catal. B Environ.* 254 (2019) 194–205; d) W. Fu, X. Guan, Z. Huang, M. Liu, L. Guo, Efficient photocatalytic overall water splitting over a core-shell GaInZnON@GaInON homojunction, *Appl. Catal. B Environ.* 255 (2019), 117741; e) Z. Ai, K. Zhang, D. Shi, B. Chang, Y. Shao, L. Zhang, Y. Wu, X. Hao, Band-matching transformation between CdS and BCNNTs with tunable p-n homojunction for enhanced photocatalytic pure water splitting, *Nano Energy* 69 (2020), 104408; f) R. Shi, H. Ye, F. Liang, Z. Wang, K. Li, Y. Weng, Z. Lin, W. Fu, C. Che, Y. Chen, Interstitial P-doped CdS with Long-lived photogenerated electrons for photocatalytic water splitting without sacrificial agents, *Adv. Mater.* 30 (2018) 1705941; g) W. Chen, G. Huang, H. Song, J. Zhang, Efficient and stable charge transfer channels for photocatalytic water splitting activity of CdS without sacrificial agents, *J. Mater. Chem. A* 8 (2020) 20963–20969; h) C. Zhu, C. Liu, Y. Zhou, Y. Fu, S. Guo, H. Li, S. Zhao, H. Huang, Y. Liu, Z. Kang, Carbon dots enhance the stability of CdS for visible-light-driven overall water splitting, *Appl. Catal. B Environ.* 216 (2017) 114–121; i) X. Song, G. Wei, J. Sun, C. Peng, J. Yin, X. Zhang, Y. Jiang, H. Fei, Overall photocatalytic water splitting by an organolead iodide crystalline material, *Nat. Catal.* 3 (2020) 1027–1033; j) X. Ning, J. Li, B. Yang, W. Zhen, Z. Li, B. Tian, G. Lu, Inhibition of photocorrosion of CdS via assembling with thin film TiO₂ and removing formed oxygen by artificial gill for visible light overall water splitting, *Appl. Catal. B Environ.* 212 (2017) 129–139.
 - [38] K.P. Lindquist, M.A. Boles, S.A. Mack, J.B. Neaton, H.I. Karunadasa, Gold-cage perovskites: a three-dimensional a_{iii}x framework encasing isolated MX₆-octahedra (MIII = In, Sb, Bi; X = Cl⁻, Br⁻, I⁻), *J. Am. Chem. Soc.* 143 (2021) 7440–7448.
 - [39] W. Li, X. Chu, F. Wang, Y. Dang, X. Liu, X. Wang, C. Wang, Enhanced cocatalyst-support interaction and promoted electron transfer of 3D porous g-C₃N₄/GO-M (Au, Pd, Pt) composite catalysts for hydrogen evolution, *Appl. Catal. B Environ.* 288 (2021), 120034.
 - [40] H. Chen, Z. Yang, X. Wang, F. Polo-Garzon, P.W. Halstenberg, T. Wang, X. Suo, S.-Z. Yang, H.M. Meyer, Z. Wu, S. Dai, Photoinduced strong metal-support interaction for enhanced catalysis, *J. Am. Chem. Soc.* 143 (2021) 8521–8526.
 - [41] a) R. Gao, J. Wang, Z.-F. Huang, R. Zhang, W. Wang, L. Pan, J. Zhang, W. Zhu, X. Zhang, C. Shi, J. Lim, Ji-Jun Zou, Pt/Fe₂O₃ with Pt-Fe pair sites as a catalyst for oxygen reduction with ultralow Pt loading, *Nat. Energy* 6 (2021) 614–623; b) T. Ricciardulli, S. Gorthy, J.S. Adams, C. Thompson, A.M. Karim, M. Neurock, D.W. Flaherty, Effect of Pd coordination and isolation on the catalytic reduction of O₂ to H₂O over PdAu bimetallic nanoparticles, *J. Am. Chem. Soc.* 143 (2021) 5445–5464.